

ARTICLE

DOI: 10.1038/s41467-017-00585-6

OPEN

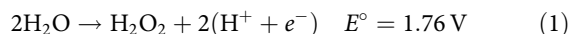
Understanding activity trends in electrochemical water oxidation to form hydrogen peroxide

Xinjian Shi ^{1,2}, Samira Siahrostami¹, Guo-Ling Li ^{3,4}, Yirui Zhang^{2,5}, Pongkarn Chakthranont¹, Felix Studt^{3,6,7}, Thomas F. Jaramillo ¹, Xiaolin Zheng ^{1,2} & Jens K. Nørskov^{1,3}

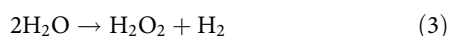
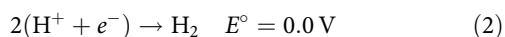
Electrochemical production of hydrogen peroxide (H_2O_2) from water oxidation could provide a very attractive route to locally produce a chemically valuable product from an abundant resource. Herein using density functional theory calculations, we predict trends in activity for water oxidation towards H_2O_2 evolution on four different metal oxides, i.e., WO_3 , SnO_2 , TiO_2 and BiVO_4 . The density functional theory predicted trend for H_2O_2 evolution is further confirmed by our experimental measurements. Moreover, we identify that BiVO_4 has the best H_2O_2 generation amount of those oxides and can achieve a Faraday efficiency of about 98% for H_2O_2 production.

¹SUNCAT Center for Interface Science and Catalysis, Department of Chemical Engineering, Stanford University, 443 Via Ortega, Stanford, CA 94305, USA. ²Department of Mechanical Engineering, Stanford University, Stanford, CA 94305, USA. ³SUNCAT Center for Interface Science and Catalysis, SLAC National Accelerator Laboratory, Menlo Park, CA 94025, USA. ⁴School of Physics and Engineering, Henan University of Science and Technology, Luoyang 471023, China. ⁵Department of Mechanical Engineering, Tsinghua University, Beijing 100084, China. ⁶Institute of Catalysis Research and Technology, Karlsruhe Institute of Technology, 76344 Eggenstein-Leopoldshafen, Germany. ⁷Institute for Chemical Technology and Polymer Chemistry, Karlsruhe Institute of Technology, 76131 Karlsruhe, Germany. Xinjian Shi, Samira Siahrostami and Guo-Ling Li contributed equally to this work. Correspondence and requests for materials should be addressed to X.Z. (email: xlzheng@stanford.edu) or to J.K.Nør. (email: norskov@stanford.edu)

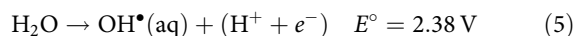
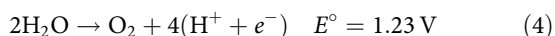
Hydrogen peroxide (H_2O_2) is an important chemical with a wide range of applications in industry, such as paper and textile manufacturing and environmental protection for detoxification and color removal of wastewater¹. Currently, H_2O_2 is produced indirectly via the anthraquinone oxidation process, which is an energy-demanding multi-electron process and requires large plants¹. Moreover, transportation of H_2O_2 to the place of use adds additional challenges due to safety concerns. Broader usage of H_2O_2 could benefit from the capability of direct on-site production. Electrochemical synthesis of H_2O_2 provides a straightforward route for on-site production and ideally solves the issues associated with the indirect anthraquinone route^{2–9}. One of the attractive possible routes for electrochemical H_2O_2 generation is via two-electron oxidation of water (Eq. 1)^{10–12}:



This process (Eq. 2) is desirable since it can be coupled with hydrogen evolution reaction (Eq. 2) to simultaneously produce two valuable products: H_2O_2 and H_2 (Eq. 3) in a single electrochemical device using only water as raw material. Such a device can also be coupled with photoabsorbers to utilize sunlight for both reactions:^{12–14}



However, the two-electron water oxidation (Eq. 1) must compete with the four-electron oxidation reaction for O_2 generation (Eq. 4) and the one-electron oxidation reaction for producing OH radical (Eq. 5)¹².



The relevant intermediates of the one- (Eq. 5¹²), two- (Eq. 1) and four-electron (Eq. 4) water oxidation reactions are OH^\bullet , O^\bullet and OOH^\bullet . Historically, the O_2 generation reaction (Eq. 4) has been the main focus of the water oxidation research^{15–29} and less attention has been paid to the selective two-electron oxidation reaction of water to H_2O_2 (Eq. 1), which is considered as a much more difficult process. A main challenge in realizing such a photoelectrochemical production of H_2O_2 system is to find a material that can selectively and efficiently produce H_2O_2 from water. Electrochemical oxidation of water has been reported over various metal oxides, such as MnO_x ^{10, 11}, WO_3 – BiVO_4 ^{14, 30, 31} and TiO_2 ^{32–36}. These pioneering works have not only demonstrated the potential of H_2O_2 production over metal oxides but also suggested that BiVO_4 is the best oxide for H_2O_2 production^{14, 31}. Nevertheless, little is known about the energy barrier and the limiting potential for H_2O_2 generation for different metal oxides. Even less is known about how the H_2O_2 generation efficiency of these metal oxides vary with applied biases both theoretically and experimentally. Such study on the bias-dependent H_2O_2 production is critical for understanding the competition among one-, two- and four-electron pathways under different bias, a prerequisite for identifying the optimal bias range for H_2O_2 generation.

In the present work, we theoretically investigate the activity trends of four different oxides (i.e., WO_3 , SnO_2 , TiO_2 and BiVO_4) towards water oxidation for H_2O_2 production with further experimental validation. Both the calculated and measured onset potentials for H_2O_2 production increase in the sequence of WO_3 , BiVO_4 , SnO_2 and TiO_2 . Among all these four oxides, BiVO_4 is

identified as the best catalyst for the two-electron water oxidation in dark and under illumination, and this result is consistent with previous studies on comparing different metal oxides for H_2O_2 production^{14, 31}. Importantly, we identify the optimal bias range for BiVO_4 to produce H_2O_2 in dark (~ 2.9 – 3.3 V vs RHE) and under illumination (~ 1.7 V– 2.3 V vs RHE). As such, BiVO_4 achieves a high faraday efficiency (FE) of 70% in dark and 98% under 1 sun illumination.

Results

Theoretical analyses. As discussed above, H_2O_2 synthesis from water oxidation is a challenging reaction. This is due to the fact that selectivity and activity of the materials are largely limited by several criteria imposed by the thermodynamics of the competing reactions¹³. The adsorption free energies of relevant intermediates of the one- (Eq. 5), two- (Eq. 1) and four-electron (Eq. 4) water oxidation reactions, i.e., OH^\bullet , O^\bullet and OOH^\bullet can be calculated using density functional theory (DFT). We show here that the free energies of OH^\bullet and O^\bullet are key parameters determining the selectivity and activity towards different oxidation products, O_2 (Eq. 4), OH radical (Eq. 5) or H_2O_2 (Eq. 1)¹³. Using DFT, we calculated the free energies of OH^\bullet , O^\bullet and OOH^\bullet on BiVO_4 (details of calculations in Supplementary Note 1). We only focus on the (111) surface, which has been shown theoretically and experimentally to be stable and exposed in the BiVO_4 crystal structure³⁷. In addition, we have taken the OH^\bullet , O^\bullet and OOH^\bullet free energies for $\text{WO}_3(100)$, $\text{TiO}_2(110)$ and $\text{SnO}_2(110)$ from reported DFT calculations (Supplementary Note 1, Supplementary Fig. 1 and Supplementary Tables 1, 2)^{13, 38–40}. We use the computational hydrogen electrode (CHE) model, which exploits that the chemical potential of a proton–electron pair is equal to gas-phase H_2 at standard conditions. The electrode potential is taken into account by shifting the electron energy by $-eU$, where e and U are the elementary charge and the electrode potential, respectively⁴¹. The limiting potential for the electrochemical reaction to occur is defined as the lowest potential, at which all the reaction steps are downhill in free energy following the previous report¹³. Figure 1 shows the activity volcano plots based on the calculated limiting potentials as a function of the calculated free energy of OH^\bullet ($\Delta G_{\text{OH}^\bullet}$) for both two-electron (black) and four-electron (blue) oxidation reactions.

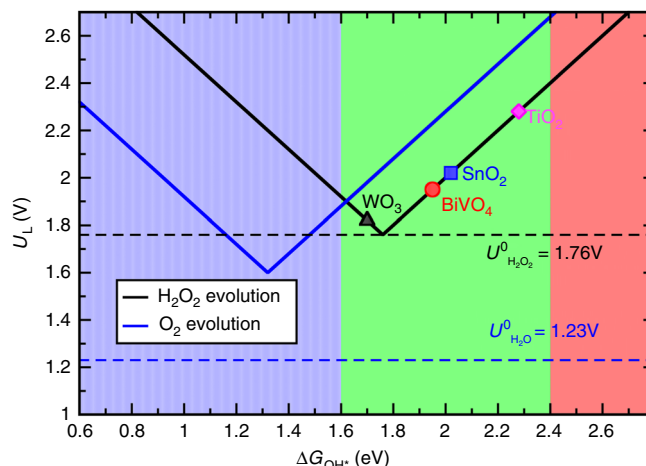


Fig. 1 Activity volcano plots. It is based on calculated limiting potentials as a function of calculated adsorption energies of OH^\bullet ($\Delta G_{\text{OH}^\bullet}$) for the two-electron oxidation of water to hydrogen peroxide evolution (black) and the four-electron oxidation to oxygen evolution (blue). The corresponding equilibrium potentials for each reaction have been shown in dashed lines

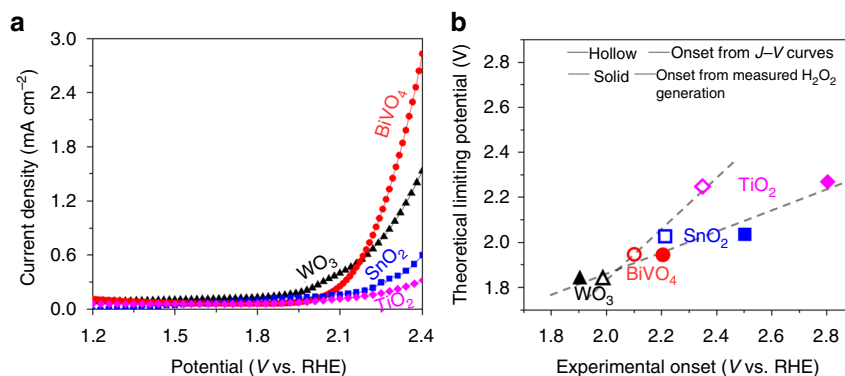


Fig. 2 *J*-*V* curves and onset potentials. **a** *J*-*V* curves of four metal oxides without illumination, for which the current onset suggest the onset of H₂O₂ production. **b** Theoretical predicted onset potentials vs experimental measured onset potentials for H₂O₂ production. The values on the y-axis are the theoretical limiting potential obtained from Fig. 1. As to the x-axis, the values of hollow points were the potentials for the *J*-*V* curves of different metal oxides to reach 0.2 mA cm⁻² in Fig. 2a, while the values of the solid points were the potentials at which the generated H₂O₂ concentration reaches 1 ppm, by measuring a 1 cm² sample in the 20 ml electrolyte for 10 min

The corresponding equilibrium potentials for each reaction have been shown in dashed lines.

From the thermodynamic point of view, materials with strong OH adsorption energy (shaded in blue in Fig. 1) will further oxidize OH* to O* and OOH*, following the complete four-electron oxidation reaction (Eq. 4) to evolve oxygen. Therefore, electrocatalysts with weak OH* free energy will have low selectivity towards the four-electron pathway but high preference towards the two-electron route. At the same time, the OH* free energy should be strong enough to dissociate the water molecule and provide a good thermodynamic driving force, for the two-electron pathway towards H₂O₂. The free energy for H₂O₂ formation is ~3.5 eV, twice of the equilibrium potential for Eq. 1, so the electrocatalyst should have $\Delta G_{O^*} \gtrsim 3.5$ eV. Given the fact that the *O and *OH energies are generally found to scale ($\Delta G_{O^*} = 2\Delta G_{OH^*} + 0.28$)³⁸, this sets a lower limit for OH* free energy, i.e., $\Delta G_{OH^*} \gtrsim \frac{3.5}{2} - \frac{0.28}{2} \sim 1.6$ eV. The upper limit for ΔG_{OH^*} is set by the free energy of OH radical formation in the solution (Eq. 5), since too weak OH* free energy with $\Delta G_{OH^*} > \sim 2.4$ eV drives the reaction towards OH radical formation (pink shaded area in Fig. 1). Hence, the combined thermodynamic criteria and scaling relation indicates a selective catalyst for H₂O₂ evolution should have ΔG_{OH^*} from ~1.6 to 2.4 eV. This thermodynamic analysis suggests that WO₃, SnO₂, BiVO₄ and TiO₂ should be able to generate H₂O₂ within certain values of the OH* free energy (shaded in green in Fig. 1). To increase the selectivity region for H₂O₂ evolution, we need to identify catalyst materials that largely deviate from the O* and OH* scaling relation⁴².

Aside from the high selectivity, the two-electron oxidation reaction (Eq. 1) ideally should also have high activity with low overpotential. The theoretical overpotential is defined as the difference between the limiting potential and equilibrium potential (1.76 V for the two-electron path). The overpotential is governed by the binding of OH* to the catalyst surface, so controlling the overpotential is a matter of tuning the free energy of OH*⁴¹. An OH* free energy (ΔG_{OH^*}) of 1.76 eV, when calculated at zero potential and relative to liquid water, will give zero overpotential. The calculated theoretical limiting potential for BiVO₄ is 1.95 V, hence it has a theoretical overpotential of ~0.2 V for the two-electron oxidation reaction. The activity of BiVO₄ can be further improved with different doped metals such as Sr and Ru (Supplementary Note 2, Supplementary Fig. 2 and Supplementary Table 3). The calculated limiting potentials for WO₃, SnO₂ and TiO₂ are 1.82, 2.02 and 2.27 V, respectively. In the following, we show that the trend in theoretical limiting

potentials for WO₃, BiVO₄, SnO₂ and TiO₂ is in very good agreement with experimental measurements.

Materials fabrication. Experimentally, we evaluate the H₂O₂ evolution performance of four oxides: WO₃, BiVO₄, SnO₂ and TiO₂ by determining their onset potentials, faraday efficiencies and production rates of H₂O₂ per geometric area of electrodes. All the oxides were synthesized on transparent and conductive fluorine-doped tin oxide (FTO) substrates. The WO₃ was synthesized by flame vapor deposition (FVD). BiVO₄, SnO₂, and TiO₂ were synthesized by a sol-gel process (see Methods and Supplementary Note 3). Since the electrochemical performance of each oxide is affected by its loading, each oxide film was individually optimized to yield the highest FE for the dark electrochemical measurement before taken for comparison. For example, Supplementary Fig. 3 shows that the measured FE for H₂O₂ production varies with the BiVO₄ loading, which was controlled by varying the precursor concentration during the spin coating process (Supplementary Fig. 4). The low loading results in low BiVO₄ coverage and exposed FTO, leading to a low H₂O₂ production. On the other hand, the high coverage results in high film resistance that impedes the charge transport process. Hence, for each oxide investigated, its loading on FTO was individually optimized for H₂O₂ production and the dependence of the FE on sample preparation conditions for each oxide is listed in Supplementary Table 4.

H₂O₂ production comparison under dark conditions. Next, we measured the current-voltage (*J*-*V*) curves for the four oxides (WO₃, BiVO₄, SnO₂ and TiO₂) without illumination (Fig. 2a). The *J*-*V* onset, as well as the experimental measured H₂O₂ evolution onset potentials (defined as the potential at which the H₂O₂ concentration reaches 1 ppm), are compared with the calculated theoretical potentials in Fig. 2b. It can be seen that both the measured current onset potential (hollow symbols) and the onset potential for H₂O₂ generation (solid symbols) increase in the order of WO₃ < BiVO₄ < SnO₂ < TiO₂, which agrees with the theoretical prediction, supporting the validity of using ΔG_{OH^*} as a descriptor to analyze the H₂O₂ evolution onset (Fig. 1). The measured onset potentials are higher than the calculated values, which is likely due to the additional kinetic barriers to be overcome in the actual experiments.

We further quantified the FE and the amount of H₂O₂ generated from the oxides as functions of the applied biases. As shown in Fig. 3a, all the metal oxides investigated share the

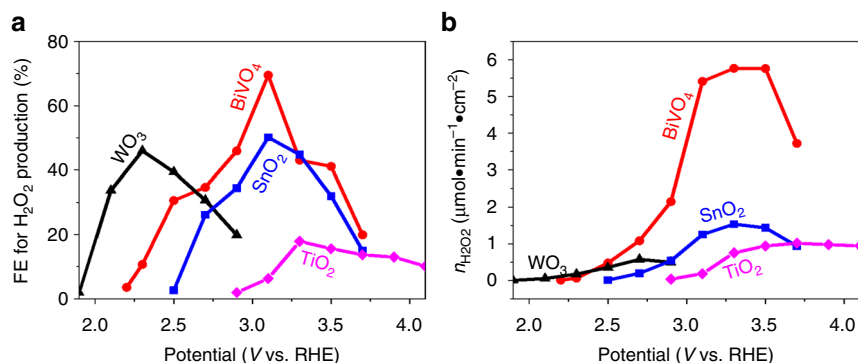


Fig. 3 The faraday efficiency (FE) and mole amount of H₂O₂ under dark. **a** The FE and **b** the mole amount (n) of H₂O₂ generation (n) vs potential (V) without illumination. Both show that BiVO₄ has the highest FE and n for H₂O₂ production over other metal oxides

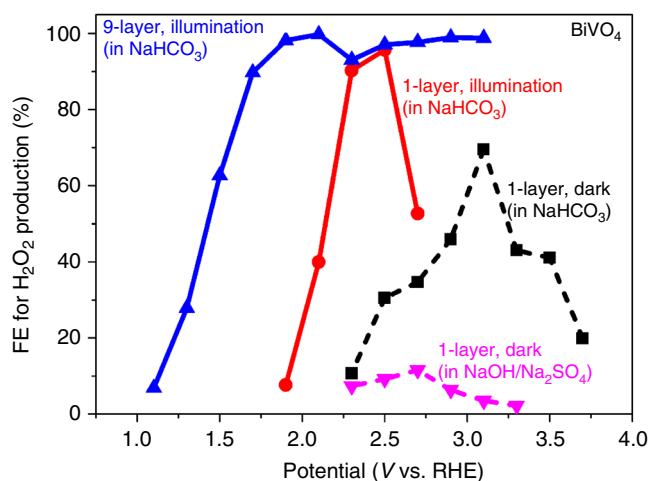


Fig. 4 The FE for BiVO₄ under both dark and illumination. FE vs applied bias for BiVO₄ under different conditions, including different electrolytes in darkness, same electrolyte between darkness and illumination, and different layers under illumination. The thicker BiVO₄ with light illumination in NaHCO₃ shows best performance for H₂O₂ production

similar FE trend with increasing applied bias: the FE first increases to a maximum value and then decreases. Or equivalently, for each metal oxide, there is an optimal potential window for H₂O₂ production, due to the competition with one-electron and four-electron oxidation reactions as predicted by theory (Fig. 1). Among all the oxides investigated, BiVO₄ achieves the highest FE of 70% at 3.1 V vs RHE. In addition, BiVO₄ also has the highest H₂O₂ production rate per geometric area of electrode (Fig. 3b), due to the combined high FE (Fig. 3a) and high current density (Fig. 2a).

H₂O₂ production on BiVO₄ under different conditions. The above results clearly indicate that BiVO₄, among the four oxides investigated, has the best electrochemical properties towards H₂O₂ production, which is consistent with the previous screening studied of different metal oxides for H₂O₂ generation³¹. Next, we further investigated the influence of other conditions on the H₂O₂ production of using BiVO₄, including the electrolyte, light illumination and sample thickness. The two dash lines in Figure 4 are the measured FEs for the thin 1-layer BiVO₄ (i.e., spin coating once) under dark using two different electrolytes: 1 M NaHCO₃ (pH = 8.3) and 0.5 M Na₂SO₄ (adjusted to pH = 8.3 with NaOH). Clearly, NaHCO₃ is a much better electrolyte than NaOH/Na₂SO₄ for the H₂O₂ production from water oxidation. This

observation is consistent with recent work by Fuku et al.,¹⁴ which reported that HCO₃⁻ is beneficial for the H₂O₂ production. In addition, as shown in Fig. 4, illumination not only shifts the onset potential to lower values but also increases the FEs for H₂O₂ production from 70% to over 95% for the 1-layer BiVO₄ in NaHCO₃. The reasons are that illumination introduces additional photogenerated charge carriers for H₂O₂ production and supplies photovoltage to allow H₂O₂ generation from water oxidation at a lower external bias⁴³. To further enhance the benefits under illumination, we increase the loading of BiVO₄ by spin coating nine times (referred as 9-layer BiVO₄) to enhance the light absorption. The increased thickness for BiVO₄ further shifts the onset potential for H₂O₂ to less than 1.1 V vs RHE, which is over 1.1 V lower than that of the dark conditions. This lowered onset potential and increased FEs strongly support that BiVO₄ is a promising photoanode material for the H₂O₂ production in a photoelectrochemical system. The J - V curve and the measured H₂O₂ generation rate under illumination for this 9-layer BiVO₄ are shown in Supplementary Fig. 5. In addition, we have measured the evolved gaseous O₂ and H₂ and the measured FEs are shown in Supplementary Fig. 6. The figure shows that the sum of the FE (O₂) and FE (H₂O₂) is about 98–103%, confirming the accuracy in our H₂O₂ concentration measurement. Finally, the photoelectrochemical stability of BiVO₄ is known to be an issue when the electrolyte is far from neutral conditions because the V⁵⁺ tends to dissolve into solution^{44, 45}. However, we used the bicarbonate electrolyte with a measured pH value of 8.3; hence, BiVO₄ is relatively stable in this near neutral region⁴⁶.

Discussion

In the present work, we utilized DFT calculations in conjunction with experimental measurements to study the activity of two-electron water oxidation towards H₂O₂ evolution over four metal oxides, namely WO₃, BiVO₄, SnO₂ and TiO₂. Both the calculated and measured onset potentials for H₂O₂ production increase in the sequence of WO₃, BiVO₄, SnO₂ and TiO₂. Among all these four oxides, BiVO₄ produces the highest faraday efficiency (~70%) and largest amount for H₂O₂ under dark. The peak faraday efficiency BiVO₄ is further increased to 98% by adding illumination, optimizing electrolyte and optimizing the thickness of BiVO₄. Those optimizations also lower the onset potential from 2.2 V to <1.1 V. These results suggest that BiVO₄ is an excellent photoanode candidate for electrochemical and photoelectrochemical H₂O₂ production. The theoretical simulation and experimental demonstration illustrated in this work have furthered the understanding of the activity and selectivity of water oxidation to H₂O₂ on metal oxide surfaces. Our result has opened an avenue for novel photoelectrochemical device designs with

fundamental mechanism study that utilize solar energy and water to produce an oxidative product with higher value beyond O₂.

Methods

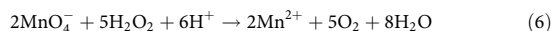
Fabrication of various metal oxides on FTO. The BiVO₄ precursor solution was prepared from a mixture of bismuth nitrate hexahydrate (BiN₃O₉·5H₂O, 99.99%; Aldrich) and vanadyl acetylacetonate (C₁₀H₁₄O₅V, 98%; Aldrich), which were added to a solution of acetylacetonate (C₅H₈O₂; Aldrich) and acetic acid (CH₃COOH, 99.70%; Fisher) with a ratio of 1:0.12, followed by sonication for 10 min. After sonication, a dark green solution was obtained and the solution is usually used within a day after the preparation. For the one named 1-layer, the mole concentration of Bi was varied from 0.08 M, and 0.04 M, 0.02 M, to 0.01 M. For a typical spin coating, 100 μl of the BiVO₄ precursor solution was dropped on a pre-cleaned FTO glass followed by spin coating (500 r.p.m. for 5 s and 1500 r.p.m. for 30 s). The samples were then annealed at 100 °C for 10 min, and 300, 400, and 500 °C for 5 min at each temperature. Similar step-wise annealing process was commonly used for metal oxide fabrication, and the purpose is to slowly evaporate the solvent to achieve a better film morphology. For spin coating multiple layers, the same process above was repeated for multiple times. Finally, the coated FTO was annealed in a box furnace at 500 °C for 2 h.

SnO₂ was fabricated by using a sol-gel process similar with BiVO₄. Firstly the precursor solution was made by dissolving 0.1932 g tin chloride in 10 ml 2-methoxyethanol (CH₃OCH₂CH₂OH, 99.8%; Aldrich) and 0.2 ml acetylacetonate (CH₃COCH₂COCH₃, ≥99.3%; Aldrich) as the best condition, and sonicated for 30 min. After then the solution was put in a fume hood with aging for one night. The solution was spin coated on top of cleaned FTO with first 5 s, 500 r.p.m. and second 35 s, 2000 r.p.m. Annealing process was carried out by using step by step method (100 °C for 5 min, 300 °C for 5 min and finally 455 °C for 30 min).

TiO₂ was fabricated from a paste making and coating process. About 9.5 ml ethanol and 0.5 ml water were mixed and 0.5 g polyethylene glycol (Aldrich) was added and the mixture was sonicated for 30 min. Then 0.25 g TiO₂ powder (Aldrich) as the best condition was added and the suspension was sonicated for another 10 min. Then the suspension was put on a hot plate and heated at 120 °C until the total volume reached 5 ml to get the TiO₂ paste. The paste was used to spin coat or blade coat on top of FTO glass, followed by the annealing process at 400 °C for 2 h.

WO₃ was synthesized by FVD method⁴⁶, for which a W wire (0.5 mm in diameter; Aldrich) was oxidized by flame as the WO_x vapor source. Those WO_x vapor further deposited on FTO as W₁₈O₄₉ nanowires. The optimized FVD condition followed the one used in Rao et al.'s work⁴⁶, with 18.4SLPM:12.5SLPM CH₄ to air flow ratio and a substrate temperature 550 °C for 10 min of deposition (Supplementary Table 4). W₁₈O₄₉ nanowires were further converted to WO₃ nanowires by annealing at 500 °C in a box furnace for 1 h.

Characterizations. The H₂O₂ production from various anodes was detected by using the potentiostat with the three-electrode system, in which the Ag/AgCl electrode was used as a reference electrode and Ti foil as the counter electrode. Silver paste and Teflon tape were used to make metal contact and to define area when necessary. The measurements under illumination were obtained under 1 Sun at AM 1.5 G. The amount of generated H₂O₂ was detected by using the standard H₂O₂ strips (Indigo Instruments). In addition, the generated H₂O₂ concentration was further confirmed with a titration process by using potassium permanganate (KMnO₄, ≥99.0%; Aldrich). The permanganate ion has a dark purple color, and the color disappears during titration when the MnO₄⁻ is totally consumed based on the following equation:



In this work, the sulfuric acid (H₂SO₄; Acros Organics) was used as the H⁺ source. We measured five H₂O₂ solution samples with different degrees of dilution from a same initial concentration 100 ppm, by both the standard strips and the permanganate titration methods. The results are shown in Supplementary Fig. 7, which shows that two methods basically agree with each other, confirming the accuracy of the H₂O₂ concentration measurement.

To make the result of the onset potential of H₂O₂ generation value more fair and accurate, in addition to the dark current onset here it was also defined as the potential at which the H₂O₂ generation starts to be detected (beyond 1 ppm), by measuring a 1 cm² sample in a 20 ml electrolyte for 10 min. H₂ and O₂ were detected by the gas chromatography analysis, and the morphology of the samples were obtained using scanning electron microscopy (FEI XL30 Sirion SEM). The FE for H₂O₂ production (%) is calculated by

$$\text{FE} = \frac{\text{Amount of generated H}_2\text{O}_2(\text{mol})}{\text{theoretical generated H}_2\text{O}_2} \times 100 \quad (7)$$

where the theoretical amount of H₂O₂ is equal to the total number of electrons divided by two (in mol). The FE of H₂O₂ is calculated based on the accumulated amount of H₂O₂ after the 10 min measurement for each condition. The FEs for H₂ and O₂ are calculated in a similar way, in which the theoretical amount of H₂ is also

equal to the total amount of electrons divided by two (in mol), while the theoretical amount of O₂ is equal to the total amount of electrons divided by four (in mol), respectively.

Computational details. Density functional theory calculations are done using the projector-augmented wave method and a plane-wave basis set as implemented in the Vienna Ab Initio Simulation Package (VASP). The valence configurations are treated as 6s²6p³ for Bi, 3d³4s² for V, 2s²2p⁴ for O and 1s¹ for H. The cutoff energy for plane-wave basis functions is 400 eV. The bulk and surface properties of BiVO₄ are optimized within GGA-PBE. For a more accurate description, the calculations are done within GGA-rPBE for the adsorption energies of OH*, O* and OOH* species on the BiVO₄(111) surface. The reference energies of the pristine slab, H₂, H₂O and O₂ molecules are also carefully treated within GGA-rPBE. For periodic slab calculations, slabs of six metal-oxygen layers are separated by at least 12 Å of vacuum. The atomic positions within the top two layers of the slabs were allowed to relax with the force convergence of 0.02 eV per Å. Spin polarization is considered in all the calculations.

Data availability. Data supporting the findings of this study are available within the article and its supplementary information files, and from the corresponding author upon reasonable request.

Received: 16 January 2017 Accepted: 7 July 2017

Published online: 26 September 2017

References

- Campos-Martin, J. M., Blanco-Brieva, G. & Fierro, J. L. G. Hydrogen peroxide synthesis: an outlook beyond the anthraquinone process. *Angew. Chem. Int. Ed. Engl.* **45**, 6962–6984 (2006).
- Siahirostami, S. et al. Enabling direct H₂O₂ production through rational electrocatalyst design. *Nat. Mater.* **12**, 1137–1143 (2013).
- Verdaguer-Casadevall, A. et al. Trends in the electrochemical synthesis of H₂O₂: enhancing activity and selectivity by electrocatalytic site engineering. *Nano Lett.* **14**, 1603–1608 (2014).
- Fellinger, T.-P., Hasché, F., Strasser, P. & Antonietti, M. Mesoporous nitrogen-doped carbon for the electrocatalytic synthesis of hydrogen peroxide. *J. Am. Chem. Soc.* **134**, 4072–4075 (2012).
- Choi, C. H. et al. Hydrogen peroxide synthesis via enhanced two-electron oxygen reduction pathway on carbon-coated Pt surface. *J. Phys. Chem. C* **118**, 30063–30070 (2014).
- Park, J., Nabe, Y., Hayakawa, T. & Kakimoto, M. Highly selective two-electron oxygen reduction catalyzed by mesoporous nitrogen-doped carbon. *ACS Catal.* **4**, 3749–3754 (2014).
- Choi, C. H. et al. Tuning selectivity of electrochemical reactions by atomically dispersed platinum catalyst. *Nat. Commun.* **7**, 10922 (2016).
- Mase, K., Yoneda, M., Yamada, Y., Fukuzumi, S. & Klug, D. R. Seawater usable for production and consumption of hydrogen peroxide as a solar fuel. *Nat. Commun.* **7**, 11470 (2016).
- Mase, K., Yoneda, M., Yamada, Y. & Fukuzumi, S. Efficient photocatalytic production of hydrogen peroxide from water and dioxygen with bismuth vanadate and a Cobalt(II) chlorin complex. *ACS Energy Lett.* **1**, 913–919 (2016).
- Izgorodin, A., Izgorodina, E. & MacFarlane, D. R. Low overpotential water oxidation to hydrogen peroxide on a MnOx catalyst. *Energy Environ. Sci.* **5**, 9496 (2012).
- McDonnell-Worth, C. & MacFarlane, D. R. Ion effects in water oxidation to hydrogen peroxide. *RSC Adv.* **4**, 30551 (2014).
- Bard, A. J., Roger, P., Hordan, J. *Standard Potentials in Aqueous Solution* (M. Dekker, 1985).
- Viswanathan, V., Hansen, H. A. & Nørskov, J. K. Selective electrochemical generation of hydrogen peroxide from water oxidation. *J. Phys. Chem. Lett.* **6**, 4224–4228 (2015).
- Fuku, K. et al. Efficient oxidative hydrogen peroxide production and accumulation in photoelectrochemical water splitting using a tungsten trioxide/bismuth vanadate photoanode. *Chem. Commun.* **52**, 5406–5409 (2016).
- Burke, M. S., Enman, L. J., Batchellor, A. S., Zou, S. & Boettcher, S. W. Oxygen evolution reaction electrocatalysis on transition metal oxides and (Oxy) hydroxides: activity trends and design principles. *Chem. Mater.* **27**, 7549–7558 (2015).
- Reier, T., Oezaslan, M. & Strasser, P. Electrocatalytic oxygen evolution reaction (OER) on Ru, Ir, and Pt catalysts: a comparative study of nanoparticles and bulk materials. *ACS Catal.* **2**, 1765–1772 (2012).
- Cheng, Y. & Jiang, S. P. Advances in electrocatalysts for oxygen evolution reaction of water electrolysis—from metal oxides to carbon nanotubes. *Prog. Nat. Sci. Mater. Int.* **25**, 545–553 (2015).

18. Diaz-Morales, O., Ledezma-Yanez, I., Koper, M. T. M. & Calle-Vallejo, F. Guidelines for the rational design of Ni-based double hydroxide electrocatalysts for the oxygen evolution reaction. *ACS Catal* **5**, 5380–5387 (2015).
19. Fabbri, E., Habereder, A., Waltar, K., Kötz, R. & Schmidt, T. J. Developments and perspectives of oxide-based catalysts for the oxygen evolution reaction. *Catal. Sci. Technol.* **4**, 3800–3821 (2014).
20. Gong, M. & Dai, H. A mini review of NiFe-based materials as highly active oxygen evolution reaction electrocatalysts. *Nano Res.* **8**, 23–39 (2014).
21. Diaz-Morales, O. et al. Iridium-based double perovskites for efficient water oxidation in acid media. *Nat. Commun.* **7**, 12363 (2016).
22. Lee, Y., Suntivich, J., May, K. J., Perry, E. E. & Shao-Horn, Y. Synthesis and activities of rutile IrO₂ and RuO₂ nanoparticles for oxygen evolution in acid and alkaline solutions. *J. Phys. Chem. Lett.* **3**, 399–404 (2012).
23. Dionigi, F. & Strasser, P. NiFe-based (oxy)hydroxide catalysts for oxygen evolution reaction in non-acidic electrolytes. *Adv. Energy Mater.* **6**, 1600621 (2016).
24. Reier, T., Nong, H. N., Teschner, D., Schlögl, R. & Strasser, P. Electrocatalytic oxygen evolution reaction in acidic environments - reaction mechanisms and catalysts. *Adv. Energy Mater.* **7**, 1601275 (2016).
25. Spoeri, C., Kwan, J. T. H., Bonakdarpour, A., Wilkinson, D. & Strasser, P. The stability challenges of oxygen evolving catalysts: towards a common fundamental understanding and mitigation of catalyst degradation. *Angew. Chem.* **56**, 5994–6021 (2017).
26. Han, B. et al. Activity and stability trends of perovskite oxides for oxygen evolution catalysis at neutral pH. *Phys. Chem. Chem. Phys.* **17**, 22576–22580 (2015).
27. Hong, W. T., Welsch, R. E. & Shao-Horn, Y. Descriptors of oxygen-evolution activity for oxides: a statistical evaluation. *J. Phys. Chem. C* **120**, 78–86 (2016).
28. Zou, S. et al. Fe (oxy)hydroxide oxygen evolution reaction electrocatalysis: intrinsic activity and the roles of electrical conductivity, substrate, and dissolution. *Chem. Mater.* **27**, 8011–8020 (2015).
29. Burke, M. S. et al. Revised oxygen evolution reaction activity trends for first-row transition-metal (oxy)hydroxides in alkaline media. *J. Phys. Chem. Lett.* **6**, 3737–3742 (2015).
30. Fuku, K. et al. Photoelectrochemical hydrogen peroxide production from water on a WO₃/BiVO₄ photoanode and from O₂ on an Au cathode without external bias. *Chem. Asian J.* **12**, 1111–1119 (2017).
31. Fuku, K., Miyase, Y., Miseki, Y., Gunji, T. & Sayama, K. Enhanced oxidative hydrogen peroxide production on conducting glass anodes modified with metal oxides. *ChemistrySelect* **1**, 5721–5726 (2016).
32. GOTO, H. Quantitative analysis of superoxide ion and hydrogen peroxide produced from molecular oxygen on photoirradiated TiO₂ particles. *J. Catal.* **225**, 223–229 (2004).
33. Hirakawa, T., Yawata, K. & Nosaka, Y. Photocatalytic reactivity for O₂- and OH radical formation in anatase and rutile TiO₂ suspension as the effect of H₂O₂ addition. *Appl. Catal. A Gen.* **325**, 105–111 (2007).
34. Cai, R., Kubota, Y. & Fujishima, A. Effect of copper ions on the formation of hydrogen peroxide from photocatalytic titanium dioxide particles. *J. Catal.* **219**, 214–218 (2003).
35. Zhang, J. & Nosaka, Y. Quantitative detection of OH radicals for investigating the reaction mechanism of various visible-light TiO₂ photocatalysts in aqueous suspension. *J. Phys. Chem. C* **117**, 1383–1391 (2013).
36. Sánchez-Quiles, D. & Tovar-Sánchez, A. Sunscreens as a source of hydrogen peroxide production in coastal waters. *Environ. Sci. Technol.* **48**, 9037–9042 (2014).
37. Li, G.-L. et al. First-principles investigation of the surface properties of fergusonite-type monoclinic BiVO₄ photocatalyst. *RSC Adv.* **7**, 9130–9140 (2017).
38. Man, I. C. et al. Universality in oxygen evolution electrocatalysis on oxide surfaces. *ChemCatChem* **3**, 1159–1165 (2011).
39. Siahrostami, S., Björketun, M. E., Strasser, P., Greeley, J. & Rossmeisl, J. Tandem cathode for proton exchange membrane fuel cells. *Phys. Chem. Chem. Phys.* **15**, 9326–9334 (2013).
40. Montoya, J. H., Garcia-Mota, M., Nørskov, J. K. & Vojvodic, A. Theoretical evaluation of the surface electrochemistry of perovskites with promising photon absorption properties for solar water splitting. *Phys. Chem. Chem. Phys.* **17**, 2634–2640 (2015).
41. Nørskov, J. K. et al. Origin of the overpotential for oxygen reduction at a fuel-cell cathode. *J. Phys. Chem. B* **108**, 17886–17892 (2004).
42. Siahrostami, S., Li, G.-L., Viswanathan, V. & Nørskov, J. K. One- or two-electron water oxidation, hydroxyl radical, or H₂O₂ evolution. *J. Phys. Chem. Lett.* **8**, 1157–1160 (2017).
43. Walsh, A., Yan, Y., Huda, M. N., Al-Jassim, M. M. & Wei, S.-H. Band edge electronic structure of BiVO₄: elucidating the role of the Bi s and V d orbitals. *Chem. Mater.* **21**, 547–551 (2009).
44. Sayama, K. et al. Photoelectrochemical decomposition of water on nanocrystalline BiVO₄ film electrodes under visible light. *Chem. Commun.* **365**, 2908 (2003).
45. Rozhkova, E. A. & Ariga, K. (eds) *From Molecules to Materials: Pathways to Artificial Photosynthesis* (Springer International Publishing, 2016).
46. Rao, P. M. et al. Simultaneously efficient light absorption and charge separation in WO₃/BiVO₄ Core/Shell nanowire photoanode for photoelectrochemical water oxidation. *Nano Lett.* **14**, 1099–1105 (2014).

Acknowledgements

We gratefully acknowledge support from the U.S. Department of Energy, Office of Sciences, Office of Basic Energy Sciences, to the SUNCAT Center for Interface Science and Catalysis. S.S. acknowledges support from the Global Climate Energy Project (GCEP) at Stanford University (Fund No.52454). G.L.L. acknowledges support from Henan University of Science and Technology (No. 2013ZCX018) and National Natural Science Foundation of China (Nos. U1404212 and 11404098). G.L.L. is grateful to the CSC scholarship.

Author contributions

J.K.N. and S.S. conceived and designed the DFT calculations. X.Z. conceived and designed the experiment. S.S. and G.-L.L. performed the DFT calculation. X.S. performed the experimental measurement. S.S., X.S. and G.-L.L. prepared the manuscript. Y.Z. and P.C. assisted on the experiment. All authors discussed the results and commented on the manuscript.

Additional information

Supplementary Information accompanies this paper at doi:10.1038/s41467-017-00585-6.

Competing interests: The authors declare no competing financial interests.

Reprints and permission information is available online at <http://npg.nature.com/reprintsandpermissions/>

Publisher's note: Springer Nature remains neutral with regard to jurisdictional claims in published maps and institutional affiliations.

 **Open Access** This article is licensed under a Creative Commons Attribution 4.0 International License, which permits use, sharing, adaptation, distribution and reproduction in any medium or format, as long as you give appropriate credit to the original author(s) and the source, provide a link to the Creative Commons license, and indicate if changes were made. The images or other third party material in this article are included in the article's Creative Commons license, unless indicated otherwise in a credit line to the material. If material is not included in the article's Creative Commons license and your intended use is not permitted by statutory regulation or exceeds the permitted use, you will need to obtain permission directly from the copyright holder. To view a copy of this license, visit <http://creativecommons.org/licenses/by/4.0/>.

© The Author(s) 2017